Applied Catalysis B: Environmental 227 (2018) 24–34

Contents lists available at ScienceDirect

Applied Catalysis B: Environmental

journal homepage: www.elsevier.com/locate/apcatb

Improved photocatalytic NO removal activity of $SrTiO_3$ by using $SrCO_3$ as a new co-catalyst

Si Jin[a,b], Guohui Dong[b,c,*], Jianmin Luo[d], Fengyun Ma[a], Chuanyi Wang[c]

[a] Key Laboratory of Coal Cleaning Conversion and Chemical Engineering Process, Xinjiang Uyghur Autonomous Region, College of Chemistry and Chemical Engineering, Xinjiang University, Urumqi, 830046, China
[b] Laboratory of Environmental Sciences and Technology, Xinjiang Technical Institute of Physics & Chemistry, Key Laboratory of Functional Materials and Devices for Special Environments, Chinese Academy of Sciences, Urumqi, 8300, China
[c] School of Environmental Science and Engineering, Shaanxi University of Science and Technology, Xian, 710021, China
[d] Xinjiang Uygur Autonomous Region Academy of Instrument Analysis, Urumqi, 830011, China

ARTICLE INFO

Keywords:
NO removal
Photocatalysis
$SrTiO_3$
Co-catalyst

ABSTRACT

In this study, $SrTiO_3$ catalyst decorated with $SrCO_3$ was prepared by one step *in-situ* pyrolysis and was used for the photocatalytic removal of NO. The presence of $SrCO_3$ not only improved the photocatalytic activity of $SrTiO_3$ but also inhibited the deactivation of $SrTiO_3$ during NO removal. In photocatalytic process, the photogenerated electrons in CB of $SrTiO_3$ could migrate to the CB of $SrCO_3$. Meanwhile, strong O_2 adsorption on the $SrCO_3$ surface would increase the production of $\cdot O_2^-$. Moreover, $SrCO_3$ could increase the surface acidity of $SrTiO_3$, which would increase the NO adsorption and facilitate the oxidation of NO. The experimental data suggested that $SrCO_3$ functions as surface deposited noble metals without the shortcomings caused by noble metals. Overall, the prepared $SrCO_3$ looks promising as environmentally friendly and economic substitute to noble metals.

1. Introduction

Acid rain, haze and photochemical smog have beenconsidered as global environmental issues, which could endanger human life and the environment [1–3]. In particular, nitrogen oxide (NOx) is one of the primary culprits leading to these problems. NOx is derived from combustion of fossil fuel, in which 95% is NO [4,5]. The increase in industrial activity releases more NO into the atmosphere [1,6,7]. To reduce hazards linked to these gases, removal of NO from the atmosphere becomes mandatory. Conventional removal approaches of NO include the selective catalytic reduction, wet scrubbing, and catalytic decomposition at high temperature (280–420 °C) [8–10]. However, these methods are applied only to environments with elevated concentrations of NO (ca. 746 ppm). The NO concentrations in the urban atmosphere or indoor air are often low that could reach parts per billion (ppb) levels [11]. This renders the above conventional approaches less effective, expensive, and complex.

Photocatalysis of polluting gases can be used for removal of NO. As shown in Fig. S3, light irradiation first causes band gap excitation to produce electrons (e^-) and holes (h^+) located at the conduction band (CB) and valence bands (VB), respectively. The photogenerated e^- and h^+ will then migrate to the surface and trigger subsequent redox reactions, which would eliminate NO during the process. Since photocatalysis of NO removal can be driven by solar energy, it can be performed under mild conditions. Meanwhile, the process is very suitable for removal of low concentration air pollutants from the atmosphere [12–17]. However, three main issues regarding the photocatalytic removal of NO require solutions. First, many photocatalysts, including bismuth-based semiconductors {$(BiO)_2CO_3$, BiOI, and Bi_2MoO_6} are vulnerable to ultraviolet or visible light irradiation [18–23]. Second, photocatalysts like g-C_3N_4 and TiO_2 oxidize NO into mainly NO_2, creating secondary pollution because NO_2 is more toxic than NO [24,25]. Three, the ultimate oxidized product (NO_3^-) cannot spontaneously leave the active sites of the catalyst, which causes poisoning. Therefore, it is of great importance to develop catalysts that are stable, efficient and reusable for NO removal.

Compared to the above-mentioned photocatalysts, strontium titanate ($SrTiO_3$) is promising for NO removal because of its numerous advantages, such as natural abundance, corrosion resistance, non-toxicity, and superior photocatalytic redox potential [26–29]. However, catalyst poisoning and rapid recombination of the photogenerated charge carriers limit its photocatalytic efficiency and application of

* Corresponding author at: Laboratory of Environmental Sciences and Technology, Xinjiang Technical Institute of Physics & Chemistry, Key Laboratory of Functional Materials and Devices for Special Environments, Chinese Academy of Sciences, Urumqi, 8300, China.
E-mail address: dongguohui@sust.edu.cn (G. Dong).

https://doi.org/10.1016/j.apcatb.2018.01.020
Received 31 October 2017; Received in revised form 23 December 2017; Accepted 8 January 2018
Available online 09 January 2018
0926-3373/

$SrTiO_3$ for NO removal. With respect to catalyst poisoning, no appropriate solutions have yet been developed. To inhibit the recombination of the photogenerated carries, noble metals like Pt, Au or Ag were deposited to extract electrons from CB of $SrTiO_3$ [30–32]. This is because noble metals with larger work functions could produce potential differences between the noble metal and $SrTiO_3$. However, noble metals are very scarce and expensive. They may also separate themselves from the surface of the photocatalyst causing secondary pollution. Due to high cost and negative impact on the environment, noble metals deposited on $SrTiO_3$ photocatalysts are not considered as eco-friendly materials (Ecomaterials). Therefore, it is urgent to develop new co-catalysts, which could not only replace noble metals but also make the modified $SrTiO_3$ are Ecomaterials.

In this study, $SrCO_3$ decorated $SrTiO_3$ was prepared by one step *in-situ* pyrolysis. The presence of $SrCO_3$ did not only improve the photocatalytic activity of $SrTiO_3$ but also inhibited the deactivation of $SrTiO_3$ during the removal of NO. Furthermore, the data indicated that $SrCO_3$ functioned similarly to surface deposited noble metals without the shortcomings caused by noble metals. The formation and catalytic mechanisms of $SrCO_3$ towards NO removal were also examined.

2. Experimental

2.1. Preparation of photocatalysts

All chemicals were of analytical grade and used without further purification. Tetrabutyltitanate (43.7 mmol) was first dissolved in 30 mL absolute ethyl alcohol, then citric acid (44.2 mmol) was added under constant stirring at room temperature to yield a solution A (Fig. S1). Meanwhile, strontium nitrate (41.2 mmol) was dissolved in 30 mL deionized water to form a solution B. Next, solution B was added to solution A to form solution C, which was kept under stirring at 343 k until forming an off-white color collosol. The obtained collosol was then dried in an oven at 353 k for 36 h. Subsequently, a pale yellow solid was obtained, which was ground into homogenous powder. Finally, the powder was placed in a crucible and annealed in air at 1173 k for different periods x (x = 0.5, 1.0, 2.0, 3.0, and 4.0) hours. The resulting powder was washed thoroughly with distilled water and ethanol then dried in an oven at 323 k. The obtained powders were denoted as Sx (x = 0.5, 1.0, 1.5 and 2.0), where x represents the calcination time.

2.2. Characterization of photocatalysts

Powder X-ray diffraction (XRD) patterns of the prepared samples were obtained using a Bruker D8 Advance diffractometer equipped with a monochromatized Cu Kα radiation (λ = 1.5408 Å). The surface area and pore size were determined by an Autosorb-IQ-MP autosorption analyzer. Before measurements, the samples were degased at 373 K for 2 h then the experiments were carried out at 77.3 K using N_2 as the adsorbate. Electron paramagnetic resonance (EPR) scans were performed on a Bruker E500 instrument, operating in the X-band at room temperature. UV–vis diffuse reflectance spectra (DRS) were scanned over the range of 200–800 nm, and recorded on a UV–vis spectrophotometer (SHIMADZU UV-1800) with integrated sphere diffuse reflectance attachment. Fluorescence spectra were monitored by a fluorescence spectrophotometer (Hitachi, Model F-7000) equipped with a PC recorder. Scanning electron microscopy (SEM) images were obtained with a ZEISS SUPRA 55VP microscope. X-ray photoelectron spectroscopy (XPS) measurements were carried out on a VG Scientific ESCALAB Mark II spectrometer equipped with two ultrahigh vacuum chambers. All binding energies were calibrated to C 1s peak at 284.6 eV of the surface adventitious carbon.

2.3. Photoelectrochemical experiments

The photocurrent experiments were performed in a three electrode quartz cells containing 100 mL of 0.1 M KCl as the electrolyte. A platinum ($1.5 \times 1.5\ cm^2$) and saturated calomel electrodes (SCE) were used as the counter and reference electrodes, respectively. The working electrodes were prepared from different catalysts following the procedure: FTO (SnO_2:F) glass substrates were first washed with distilled water and ethanol in an ultrasonic cleaner for 30 min. Next, 10 mg of catalyst slurry obtained by dispersing the catalyst in 0.5 wt% α-naphthol solution followed by grinding for 10 min was loaded onto the pretreated FTO glass substrate ($1.5 \times 1.5\ cm^2$). The electrode was then dried at 150 °C in the air to form the photoelectrode. A 300 W xenon lamp was used as a light source and kept at a distance of 15 cm away from the photoelectrode.

2.4. Photocatalytic removal of NO

The photocatalytic removal of NO was tested over different Sx samples under ultraviolet and visible light irradiations. The experiments were carried out at room temperature in a cylindric continuous-flow reactor ($\pi \times R^2 \times H = 0.785$ L, R = 5 cm, and H = 10 cm) made of Pyrex glass containing a roof quartz window. A circular glass sample dish (R = 3 cm) containing 50 mg Sx was placed in the middle of the reactor. A 300 W Xe lamp with 420 nm cutoff filter was used as the simulated visible light source, which was vertically placed above the reactor so that the sample dish could directly accept the incident light.

2.5. Scavenging experiments

In general, photocatalytic reactions involve various active species, such as photogenerated electrons (e^-), holes (h^+), superoxide ($\cdot O_2^-$), and hydrogen peroxide (H_2O_2). Comparative investigations of the effects induced by these species on photocatalysis were performed using scavenger agents to remove the species. Potassium iodide (KI), potassium dichromate ($K_2Cr_2O_7$) and *tert*-butyl alcohol (TBA) were employed as scavengers for h^+, e^- and ·OH, respectively. Typically, 50 mg photocatalyst was mixed with 1 mmol trapping agent in 10 mL H_2O. The mixtures were ultrasonicated for 15 min then the aqueous suspensions were coated onto glass dishes followed by drying at 60 °C until the water was completely evaporated. The coated dishes were used for photocatalytic removal of NO as described above.

3. Results and discussion

3.1. XRD characterization

X-ray diffraction (XRD) measurements were used to investigate the crystal structures of the results samples. Fig. 1a indicated that the catalysts without thermal treatment showed numerous peaks, which could well be indexed to $Sr(NO_3)_2$ (JCPDS no. 25-746). According to previous reports, $Ti(OBu)_4$ could change into $Ti(OH)_4$ after hydrolysis. However, $Ti(OH)_4$ cannot be detected at this stage may be because Ti^{4+} was chelated by citric acid to yield citric acid titanium chelate ($Ti(C_6H_6O_7)_2$). After the calcination of the precursor at 900 °C for 0.5 h, the peaks of $Sr(NO_3)_2$ vanished from the spectra. Meanwhile, peaks related to $SrCO_3$ appeared in the XRD pattern (Fig. 1b), indicating that $Sr(NO_3)_2$ preferentially reacted with excess citric acid to form intermediate products ($SrCO_3$). Extending the calcination time from 0.5 h to 1 h decreased the intensity of $SrCO_3$ peaks and formed new peaks related to $SrTiO_3$ (Fig. 1b). In this regard, $SrTiO_3$ may be formed from the reaction between $SrCO_3$ and $Ti(C_6H_6O_7)_2$. Further increase in calcination time to 2 h fully removed the characteristic diffraction peaks of $SrCO_3$, and pure $SrTiO_3$ was formed (Fig. 1b). Thus, it could be concluded that formation of pure $SrTiO_3$ was preceded by complexes of $SrTiO_3$ and $SrCO_3$.

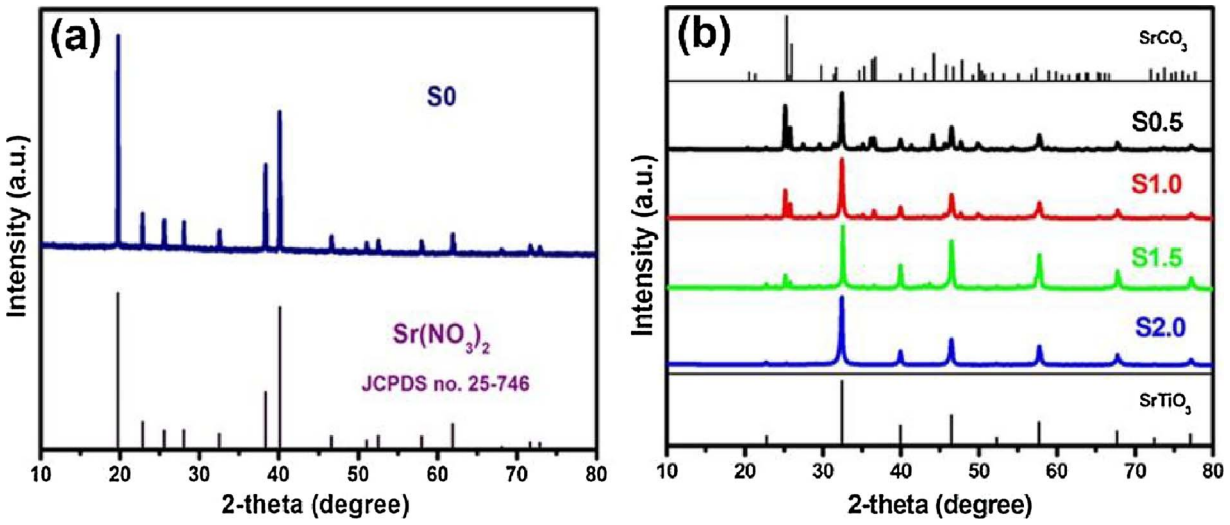

Fig. 1. XRD patterns of the $Sr(NO_3)_2$ (a), Sx samples (b).

3.2. Formation mechanism of Sx

To clarify the formation mechanism of Sx, Thermo gravimetric analysis (TGA) was employed to analyze the weight and heat changes of the precursor (Dried collosol) during the calcination process. TGA was carried out under a nitrogen atmosphere from 20 to 950 °C at a heating rate of 10 °C min^{-1}. Fig. 2a presented four continuous weight-losses in the range of the tested temperatures. The differential scanning calorimeter (DSC) curve also presented several endothermic and exothermic peaks. In the first stage, the mass loss (ca. 37%) might be assigned to dehydration of the precursors and decomposition of superfluous citric acids. Because these processes required heat absorption from the environment, DSC showed an endothermic peak. The second weight-loss (ca.13%) appeared in the temperature range of 380–600 °C, with two endothermic peaks, implying the occurrence of two reactions. These data combined with those from XRD (Fig. 1b) suggested that the endothermic peak at 420 °C could correspond to the formation of $SrCO_3$ when $Sr(NO_3)_2$ reacted with citric acid or CO_2, while the weak endothermic peak at 558 °C was linked to the crystallization process of $SrCO_3$. In the third stage, the DSC curve presented an exothermic peak at 628 °C while TG curve showed a sudden weight-loss at the same temperature. The weight and heat changes after the third stage appeared not so obvious. This suggested that the formation of $SrTiO_3$ occurred during the third stage, accompanying the burn out of the organic ligands (In $Ti(C_6H_6O_7)_2$).

To further confirm the formation process of $SrTiO_3$, the precursors were calcined at 300 °C, 558 °C and 628 °C, respectively. These calcination temperatures were derived from the ranges corresponding to the first three stages in TGA curves. The calcination of the precursors at 300 °C (Fig. 2b) showed the powders with remained $Sr(NO_3)_2$, confirming that the first stage of mass loss attributed to dehydration of the precursors and decomposition of superfluous citric acids. When the calcination temperature was increased to 558 °C, the powders turned into $SrCO_3$, consistent with the TGA analyses. Further increase in calcination temperature to 628 °C eliminated part of $SrCO_3$ and formed $SrTiO_3$, in accordance with TGA analyses stating that the formation of $SrTiO_3$ occurred during the third stage. Based on the above experimental results and analyses, the formation of $SrTiO_3$ may involve the following steps:

$$Ti(OBu)_4 + 2C_6H_8O_7 \rightarrow Ti(C_6H_6O_7)_2 + 4C_4H_9OH \quad (1)$$

$$2C_6H_8O_7 + 9O_2 \xrightarrow{160-180^{\circ}C} 12CO_2\uparrow + 8H_2O\uparrow \quad (2)$$

$$2CO_2 + 2Sr(NO_3)_2 \xrightarrow{380-600^{\circ}C} 2SrCO_3 + 4NO_2\uparrow + H_2O\uparrow \quad (3)$$

$$Ti(C_6H_6O_7)_2 + SrCO_3 + 3O_2 \xrightarrow{600-680^{\circ}C} SrTiO_3 + 7CO_2\uparrow + 6H_2O\uparrow \quad (4)$$

The SEM images of Sx at the same magnifications are shown in Fig. 3. The S0.5 sample ($SrCO_3$) showed self-assembled nanoparticles with the presence of nano-pores (Fig. 3a). Fig. 3b illustrates the morphology of S1.0, prepared as S0.5, which obtained by extending calcination time from 0.5 to 1.0 h. The nano-pores observed in S0.5 vanished

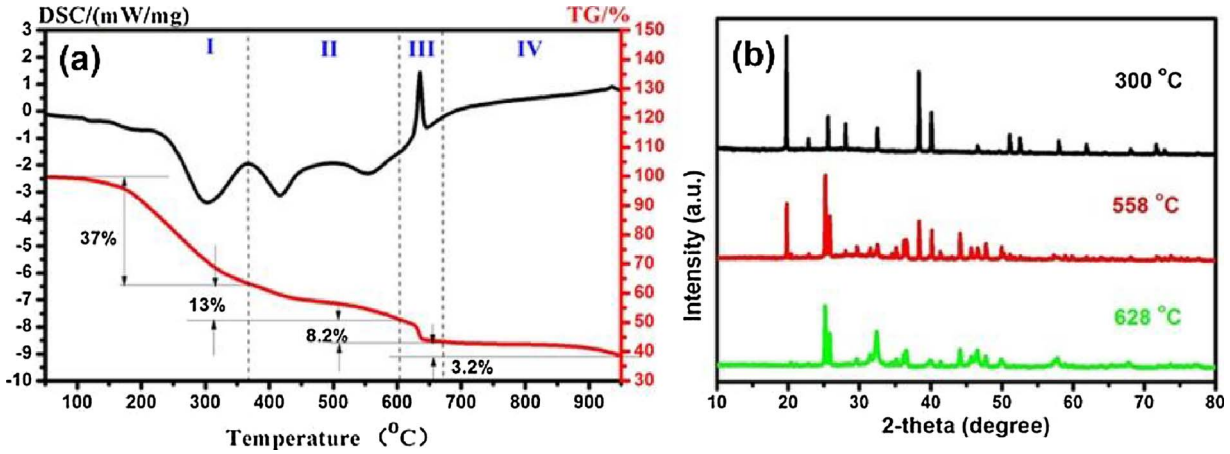

Fig. 2. TGA curves of the precursor (a); XRD patterns of the precursors calcined at 300 °C, 558 °C and 628 °C (b).

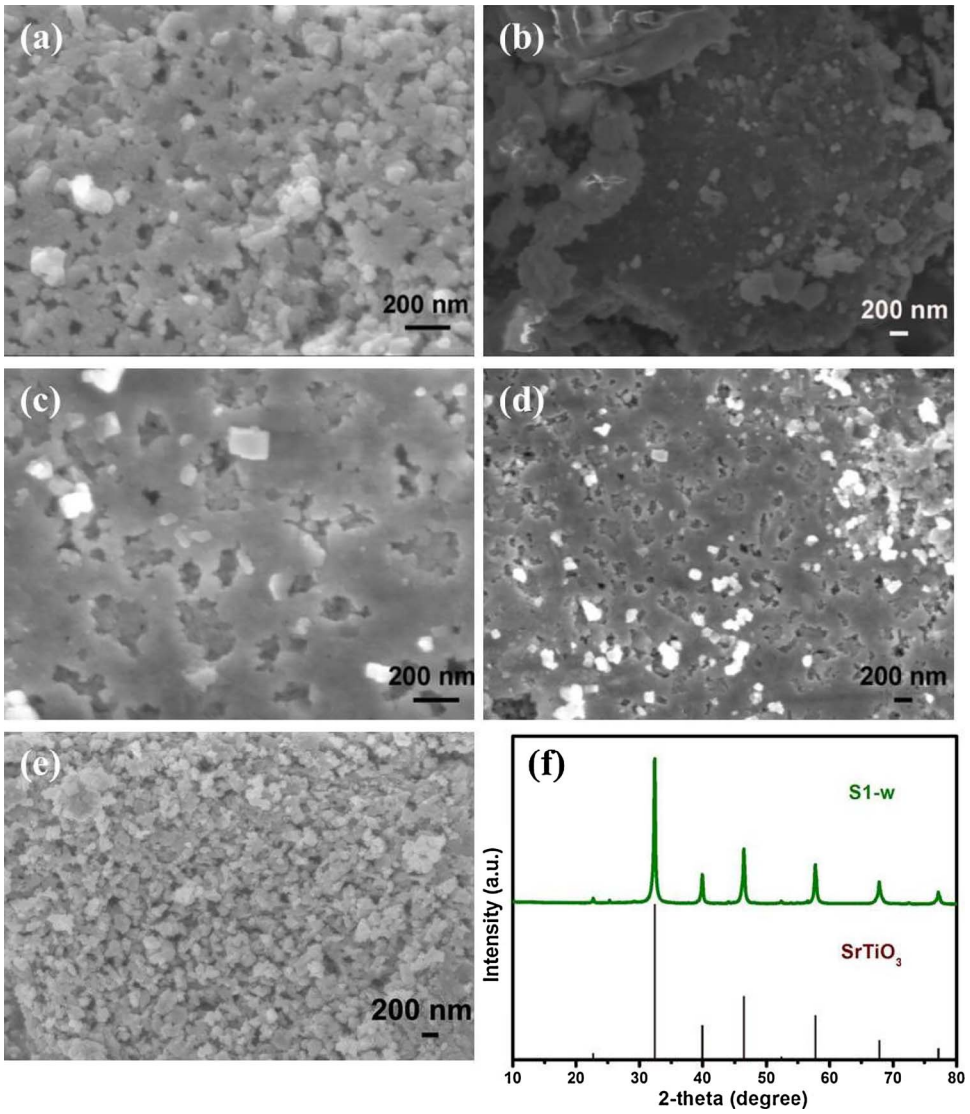

Fig. 3. SEM images of S0.5 (a), S1.0 (b), S1.5 (c), S2.0 (d), S1.0w (e) and XRD pattern of the S1.0w (f).

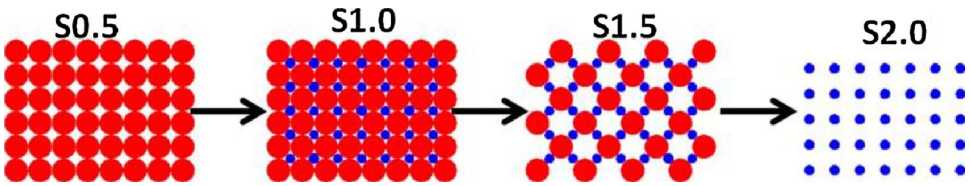

Fig. 4. The change mechanism of the morphology of Sx; the red spot represent $SeCO_3$; the blue spot represent $SrTiO_3$. (For interpretation of the references to colour in this figure legend, the reader is referred to the web version of this article.)

in S1.0, which could be related to the formation of $SrTiO_3$ occupying the nano-pores. Further extension of calcination time regenerated nanoporous structure (Fig. 3c and d), which could be caused by the decomposition of $SrCO_3$. These two phenomena suggested that the newly formed $SrTiO_3$ could alternately be rearranged in the pores of $SrCO_3$. To confirm this speculation, S1.0 was washed with dilute nitric acid to remove $SrCO_3$. The removal of $SrCO_3$ can be proved by XRD analysis as shown in Fig. 3f. As shown in Fig. 3e, the washed S1.0 (denoted as S1.0w) displayed many nano-pores similar to the morphology of S1.5. Based on above SEM results and analyses, the changing morphology of Sx is summarized in Fig. 4.

3.3. Photocatalytic activity and stability

The photocatalytic oxidation of NO using Sx was carried out in the continuous-flow cylindrical reactor. During the photocatalytic process, a 300 W Xe lamp was employed as the source for simulating the solar light. In absence of photocatalysts or light irradiation, NO was stable and cannot be removed under light irradiation (Fig. 5a). In presence of the catalyst, NO was gradually removed under light irradiation, indicating that all Sx possessed photocatalytic activities towards the removal of NO. Among them, S1.0 catalyst exhibited the optimal activity, with 47% removal efficiency after 12 min irradiation. Since S1.0 contained $SrCO_3$ and $SrTiO_3$, the catalytic activities of pure $SrCO_3$ and pure $SrTiO_3$ were also evaluated. As shown in Fig. 5b, pure $SrCO_3$ did not show any catalysis of NO removal under the same photo-irradiation conditions. This was caused by the large band gap of $SrCO_3$, which cannot be excited. To yield pure $SrTiO_3$, S1.0 was washed several times with 0.1 M HNO_3 and deionized water. XRD confirmed that the washed sample was pure $SrTiO_3$ (Fig. 3f). In turn, this washed sample had a weaker catalytic activity than S1.0 (Fig. 5b). More importantly, the washed sample presented serious deactivation during the

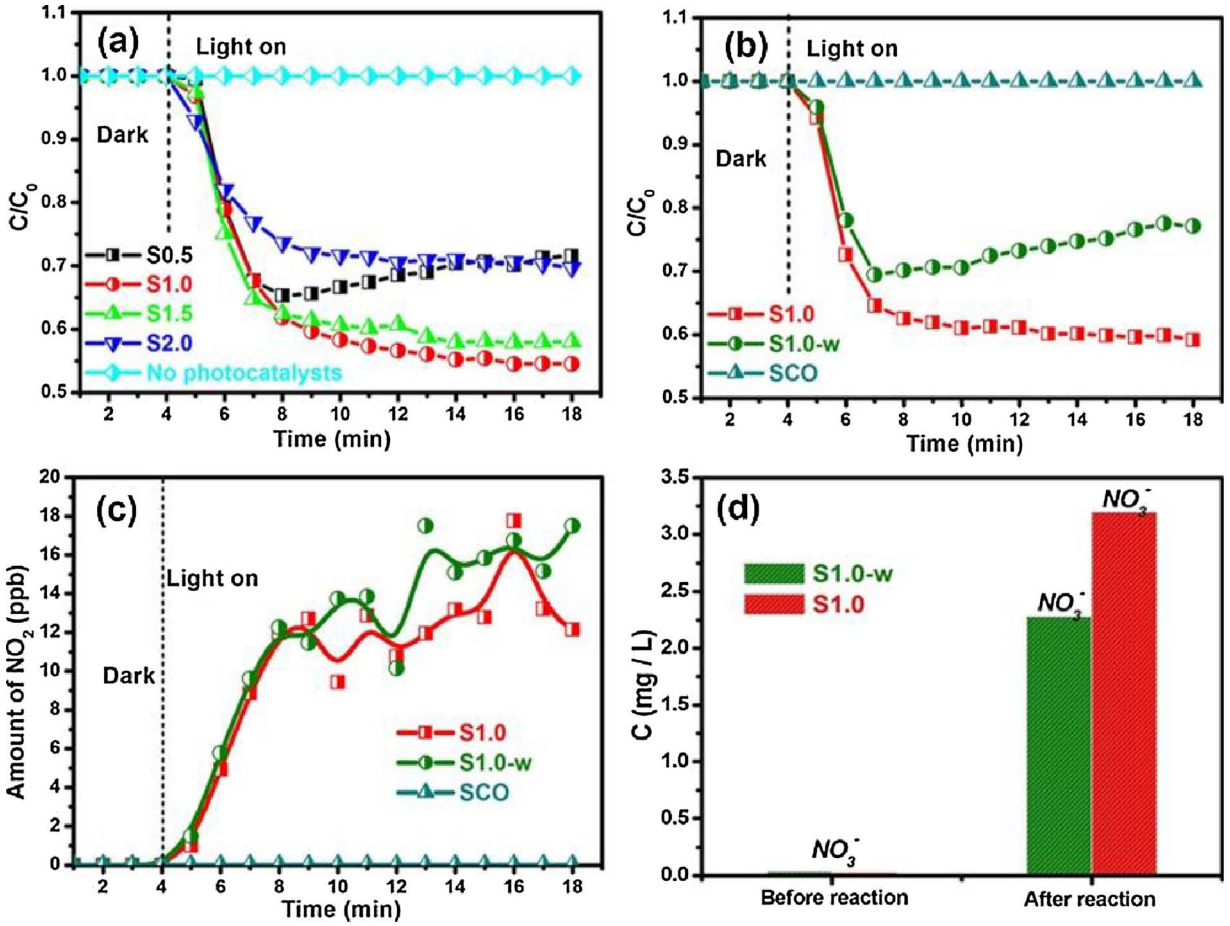

Fig. 5. The relative change in NO concentration (C/C_0) as a function of irradiation time tested over Sx samples (a) and (b); NO_2 concentration changing with irradiation time tested over S1.0, S1.0w and $SrCO_3$ (C); Ion chromatography analysis of S1.0 and S1.0w before and after reaction (d).

photocatalytic process. These data suggested that $SrCO_3$ did not only improve the photocatalytic activity of $SrTiO_3$ but also inhibited the deactivation of $SrTiO_3$ during the NO removal process.

Besides NO, the produced NO_2 during the photocatalysis was also evaluated. The generated concentrations of NO_2 using S1.0w and S1.0 were very low because both catalysts may facilitate the deep oxidation of NO into NO_3^- or NO_2^- (Fig. 5c), as confirmed by ion chromatography analysis. Compared to eluents of the initial S1.0w and S1.0, the eluents of used samples exhibited large amount of NO_3^- (Fig. 5d). This suggested that the main products in both S1.0w and S1.0 systems were NO_3^-.

Meanwhile, the recyclability and stability of the photocatalysts are important for practical applications. In general, the generated NO_3^- could deactivate the catalysts because it could easily occupy the active sites. Therefore, the cycling performances of the catalysts towards the photocatalytic removal of NO using S1.0 and S1.0-w were evaluated. After 5 repeated runs, the NO removal effect of S1.0-w decreased from 42% to 22% (Fig. 6a). This could be caused by poisoning of the active sites. However, the effect of NO removal over S1.0 did not decline (Fig. 6b). The excellent stability of S1.0 further indicated that $SrCO_3$ could suppress the poisoning effect of the active sites. Detail reasons will be analyzed later.

3.4. Optical properties

The photogeneration of carriers is the most step in the photocatalytic removal of NO. To identify why $SrCO_3$ could improve the photocatalytic activity of $SrTiO_3$, the generation process of carriers was examined for S1.0, S1.0w, and $SrCO_3$. The photogeneration of carriers involves light absorption, semiconductor photoexcitation, and separation of the photoinduced charge carriers. The light absorption and semiconductor photoexcitation strongly depend on the band gap (*Eg*) of the photocatalyst. UV–vis diffusion reflectance spectrometry (DRS) was employed to estimate the light absorption ability and band gap energy of the different catalysts. The absorption edges of S1.0, S1.0w and $SrCO_3$ were estimated to nearly 395, 385 and 250 nm, respectively (Fig. 7a). Compared to absorbance of S1.0 and S1.0w from 200 to 400 nm, the absorbance of $SrCO_3$ was negligible. The band gap energy values of S1.0, S1.0w and $SrCO_3$ were calculated as 3.0, 2.9 and 4.9 eV, respectively (Fig. 7b). Both the absorbance and band gap suggested that the presence of $SrCO_3$ did not help the photoexcitation of $SrTiO_3$.

The generated electrons and holes then migrate to the surface of the photocatalyst to start the removal process of NO. More surface carriers will induce higher photocatalytic activities. Since the photocurrent is related to the number of surface carriers, the photocurrents induced by the catalyst were estimated to compare the number of surface carriers. As shown in Fig. 7c, the photocurrent generated by S1.0 was significantly higher than that induced by S1.0w. This undoubtedly indicated that S1.0 produced more surface carriers. The higher generated surface carriers may be explained by two possible reasons. First, $SrCO_3$ could help $SrTiO_3$ to produce extra photogenerated carriers. However, the DRS results indicated that $SrCO_3$ could not be excited to produce extra photogenerated carriers because its band gap was too big. Moreover, it could not help the photoexcitation of $SrTiO_3$. Thereby, this possibility was ruled out. Second, $SrCO_3$ can improve the separation between the photoinduced charge carriers of $SrTiO_3$. To probe this possibility, photoluminescence (PL) emission spectroscopy was carried out to survey the separation of the photoinduced charge carriers during

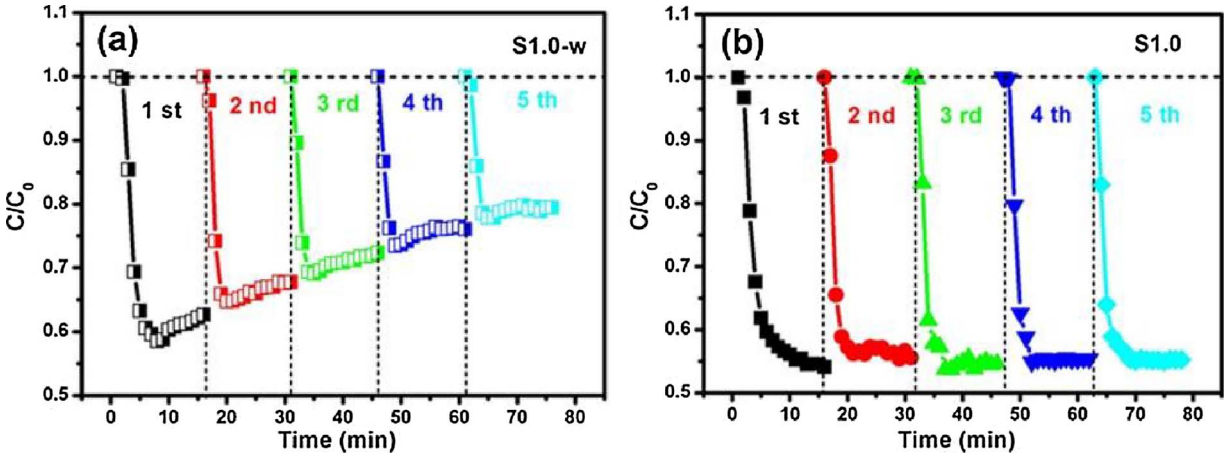

Fig. 6. The stability of S1.0w (a) and S1.0 (b) in multiple runs of NO removal.

photocatalysis. Since the emission peak is derived from recombination of electrons and holes, enhanced charge carrier separation should give rise to low-intensity emission peak. As shown in Fig. 7d, all PL spectra of Sx exhibited an emission peak at 600 nm, with variable intensities among the samples. Compared to S1.0w and $SrCO_3$, S1.0 showed the lowest emission peak, confirming the introduction of $SrCO_3$ over $SrTiO_3$ can improve the separation of the photoinduced charge carriers in $SrTiO_3$, producing more surface carriers.

To further clarify the improvement process of carrier separation, the potentials of both valence and conduction bands of the catalysts were investigated by Mott–Schottky plots. Both $SrTiO_3$ and $SrCO_3$ showed positive slopes (Fig. 8a), suggesting n-type semiconductors. The x-axis intercept of the tangent can be used to determine the flat-band potential (V_{fb}). The V_{fb} of $SrTiO_3$ and $SrCO_3$ were estimated to −1.4 and −0.95 eV (versus SCE), respectively. In n-type semiconductors, the conduction band potential (Ec) is equivalent to V_{fb}. Therefore, Ec of $SrTiO_3$ and $SrCO_3$ were estimated to −1.4 and −0.95 V (versus SCE), respectively. Since the band-gap (Eg) is the difference between the valence band potentials (Ev and Ec), Ev of $SrTiO_3$ and $SrCO_3$ were calculated as 1.6 and 3.93 V using the formula: Ev = Eg + Ec.

Based on the band potential data, the band structure diagram of S1.0 was presented to analyze the separation process of charge carriers.

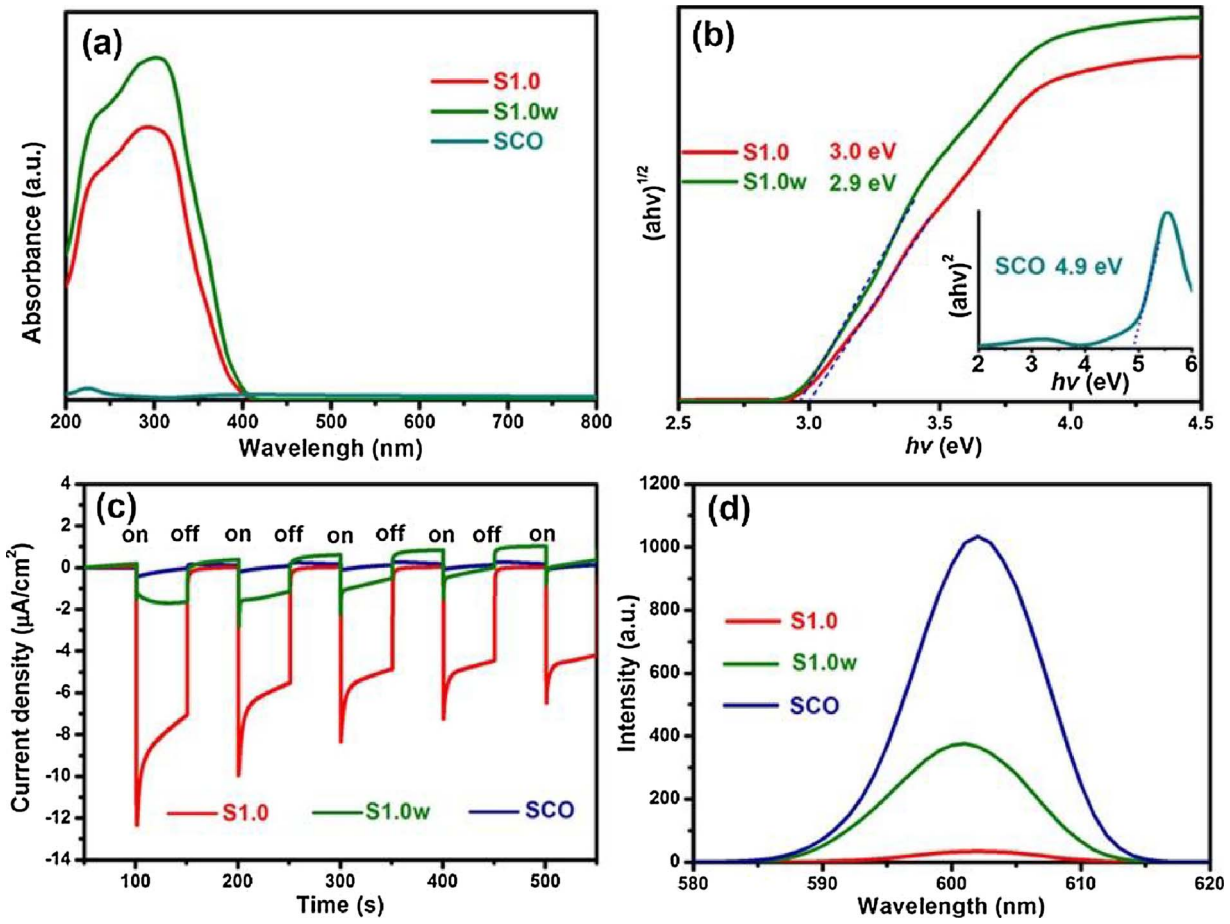

Fig. 7. UV–vis absorption spectra (a); The plots of $(ahv)^2$ versus energy (hv) (b); Current-time curves (c); PL spectra (d) of S1.0, S1.0w and $SrCO_3$.

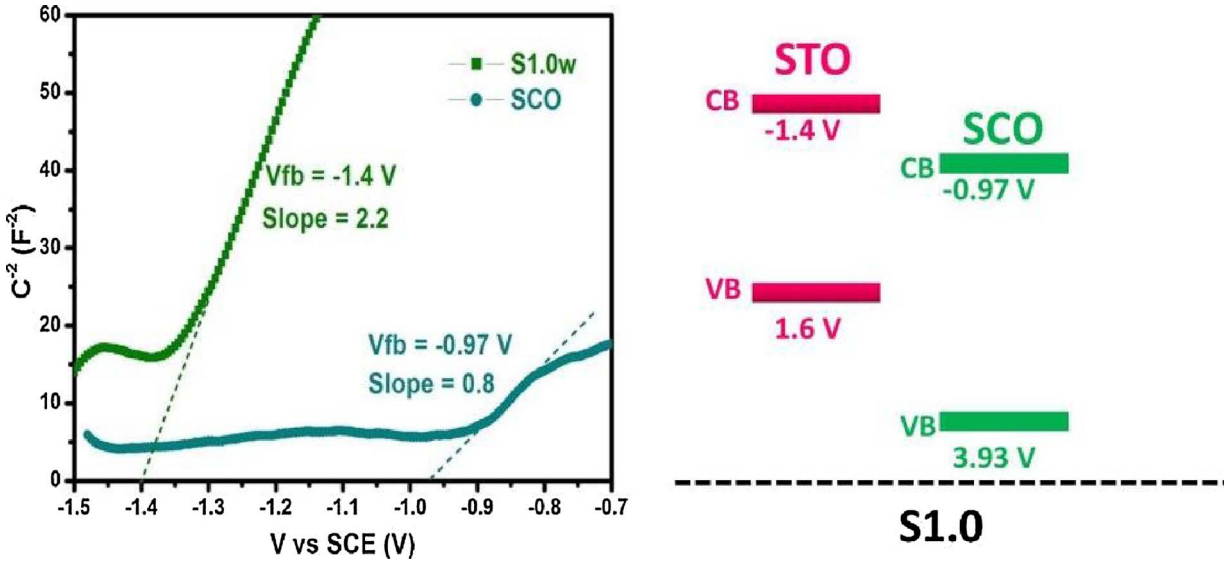

Fig. 8. Mott-Schottky plot of $SrTiO_3$ and $SrCO_3$ (a); The band structure diagram of $SrTiO_3$ (STO) and $SrCO_3$ (SCO) (b).

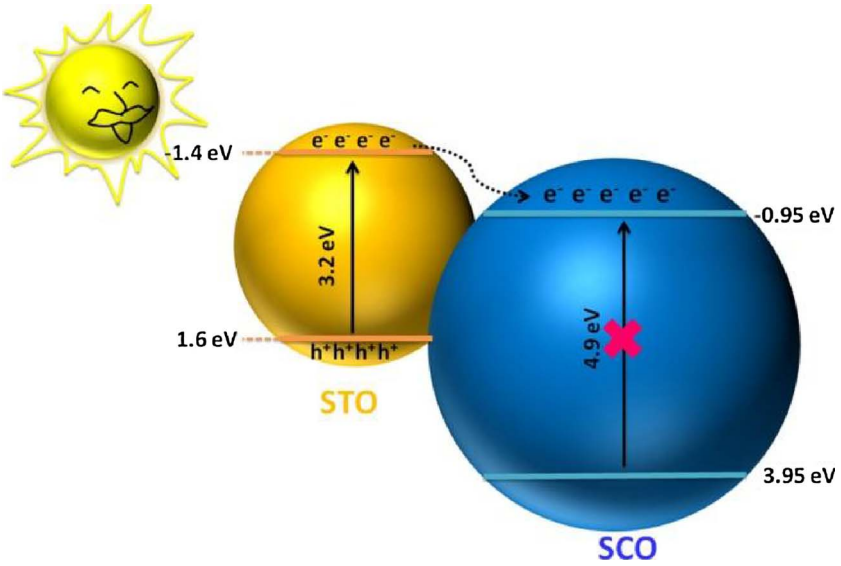

Scheme 1. Photocatalysis mechanism of $SrTiO_3$ decorated with $SrCO_3$ under light irradiation.

Fig. 8b indicated that both VB and CB of $SrTiO_3$ were higher than those of $SrCO_3$. Thus, the photogenerated electrons in CB of $SrTiO_3$ could migrate to the CB of $SrCO_3$ though $SrCO_3$ could not be excited in the present proposed system. Meanwhile, the photogenerated holes occupy the VB of $SrTiO_3$. Scheme 1 depicts the charge separation in S1.0, suggesting that S1.0 produced more photogenerated electrons and holes to drive the NO removal process.

3.5. Active species trapping

Using photocatalysis, pollution can directly be removed by redox reactions induced by photogenerated holes and electrons. These holes and electrons may also produce many oxidizing species, such as $\cdot O_2^-$, H_2O_2 and ·OH to indirectly start the removal process. To clarify the process, a series of active species trapping experiments were performed. Fig. 9a and b revealed that the addition of *tert*-butyl alcohol (TBA), which is a hydroxyl radical scavenger [33], did not depress the NO removal rate using S1.0 and S1.0w catalysts. This indicated that ·OH was not an active species in the NO removal process. By contrast, the addition of potassium iodide (KI), which is an hole scavenger [34], almost depressed the NO removal using S1.0 and S1.0w catalysts, suggesting that the photogenerated holes were indispensable for NO removal. When silver nitrate ($AgNO_3$) was used as an electron scavenger, the NO removal using S1.0 and S1.0w were significantly depressed. P-benzoquinone (PBQ), a superoxide radical scavenger [35], showed the same effect as $AgNO_3$ using both catalysts. $\cdot O_2^-$ is often generated from the direct reduction of O_2 ($O_2 + e^- \rightarrow \cdot O_2^-$), and the presence of $\cdot O_2^-$ could be monitored by EPR measurements (Fig. 9c). Therefore, $\cdot O_2^-$ may replace electrons to directly participate in the NO removal reaction. Since both the photogenerated hole and $\cdot O_2^-$ were indispensable, they may play a synergic role in the NO removal. According to our previous report, NO could be oxidized into NO^+ by photogenerated hole. Based on the above analysis, NO removal process using S1.0 can be expressed by the following steps:

$$S1.0 + light \rightarrow h^+ + e^- \quad (5)$$

$$NO + h^+ \rightarrow NO^+ \quad (6)$$

$$e^- + O_2 \rightarrow {}^{\circ}O_2^- \quad (7)$$

$$NO^+ + {}^{\circ}O_2 \rightarrow NO_3^- \quad (8)$$

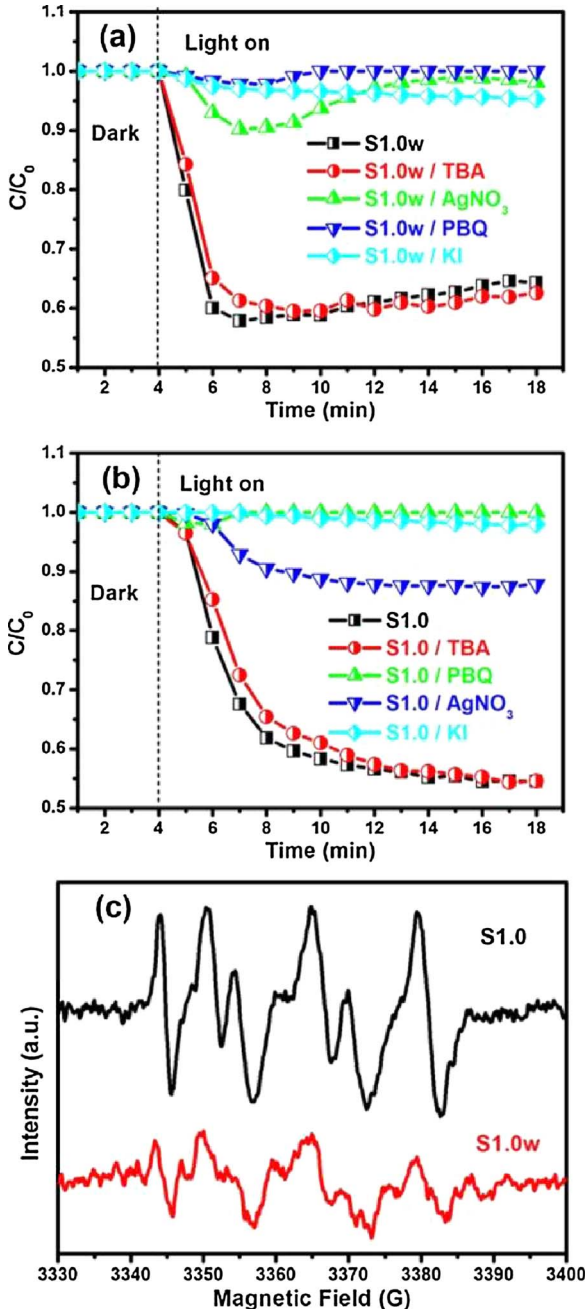

Fig. 9. Influence of different scavengers (TBA for ·OH, $AgNO_3$ for e^-, PBQ for $\cdot O_2^-$, KI for h^+) using S1.0w (a) and S1.0 (b); ESR signals of DMPO- $\cdot O_2^-$ spin adduct of the S1.0w and S1.0 under visible light illumination for 5 min.

3.6. TPD analysis of NO adsorption-Desorption

Since the photocatalytic removal process of NO is heterogeneous, adsorption is necessary for efficient catalysis. Also, because NO removal involves the participation of $\cdot O_2^-$, temperature-programmed desorption (TPD) was employed to gain a better understanding of the adsorption states of NO and O_2 on the surface of S1.0. Fig. 10a illustrated that NO desorption curves of S1.0 and S1.0w had similar peaks at the same temperature of 530 °C, implying similar NO adsorption sites in S1.0 and S1.0w. Therefore, NO was mainly adsorbed on the $SrTiO_3$ section of S1.0. Moreover, the peak in S1.0w appeared weaker than that of S1.0, indicating that $SrCO_3$ could increase the NO adsorption ability of $SrTiO_3$. This could be related to the fact that $SrCO_3$ can increase the surface acidity of $SrTiO_3$. Since the photogenerated holes were left in VB of $SrTiO_3$, NO adsorption on $SrTiO_3$ would facilitate the direct oxidation of NO induced by the photogenerated holes.

Besides NO-TPD, O_2-TPD was also investigated because the O_2 reduction reaction was involved in NO removal process. As shown in Fig. 10b, only one O_2 desorption peak was present in the S1.0w curve at about 320 °C. However, when $SrTiO_3$ was combined with $SrCO_3$, a new strong O_2 desorption peak appeared in S1.0 at about 600 °C. These observations suggested that O_2 could more likely be adsorbed on $SrCO_3$ though it could be adsorbed on both $SrTiO_3$ and $SrCO_3$ catalysts. This appeared reasonable because $SrCO_3$ could act as Lewis acid while O_2 is a typical Lewis base. Scheme 1 indicated that the photogenerated electrons in $SrTiO_3$ can migrate to the $SrCO_3$. Thus, strong O_2 adsorption on the $SrCO_3$ surface would increase the reduction of O_2, which, in turn, would produce more $\cdot O_2^-$ by S1.0 to further oxidize NO^+.

It is widely accepted that the adsorption state of the adsorbate depends on the surface atomic structure of the adsorbent. Fig. 11 presented two kinds of atomic terminations (O and Sr) on the surface of $SrTiO_3$. Both O and Sr terminations have single electrons, likely to form covalent bonds with other atoms with single electrons. However, the electronegativity of O termination (3.5) is much large than that of Sr terminations (1.0), suggesting that O termination is easier to form covalent bonding than Sr termination. The previous report showed the nitrogen atom of NO to have unpaired electron. Therefore, NO would preferentially adsorb on the O termination of $SrTiO_3$ through the formation of covalent bonding between the O termination of $SrTiO_3$ and nitrogen atom of NO. When NO was oxidized to NO^+, the unpaired electron of N was used by the photogenerated hole of $SrTiO_3$. Hence, NO^+ would leave O termination of $SrTiO_3$ to find new adsorption site. The N and O atoms of NO^+ have lone-pair electrons while the Sr termination of $SrTiO_3$ has empty 5p orbital. This would make NO^+ preferentially adsorb on Sr termination of $SrTiO_3$ through the formation of coordination bond. In NO^+, the electronegativity of N atom (3.0) is smaller than that of O atom (3.4). Therefore, N atom of NO^+ would form the coordination bond with Sr termination of $SrTiO_3$ much easier.

The above analyses suggested that $\cdot O_2^-$ would play a significant role in NO removal. Therefore, the co-adsorption state of O_2 should be considered. Similar to NO^+, O_2 also has lone-pair electrons and should preferentially adsorb on Sr termination through the coordination bond. On pure $SrTiO_3$, O_2 should be adsorbed on Sr termination when NO was adsorbed on the O termination (Fig. 12). The adsorbed O_2 and NO were then reduced or oxidized to $\cdot O_2^-$ and NO^+, respectively. After this step, NO^+ should leave the O termination and move to the Sr termination (Fig. 13). Hence, NO^+ may react with $\cdot O_2^-$ to form NO_3^- in the Sr termination, resulting in the poisoning of O_2 adsorption sites by the produced NO_3^-. This, in turn, resulted in the poor stability of $SrTO_3$ during the removal of NO.

Different from $SrTiO_3$, the O_2 adsorption sites on S1.0 were mainly distributed in the $SrCO_3$ section, which could prevent the poisoning of O_2 adsorption sites. Thus, the final products (NO_3^-) obviously did not affect the absorption and reaction of fresh NO and O_2. As a result, NO removal activity of S1.0 appeared very stable during the subsequent processes. Overall, S1.0 showed great potential for practical applications.

3.7. Advantage analysis

Previous reports suggested that surface deposition of noble metals improve the NO removal activity of photocatalysts. Deposited noble metals, such as Pt and Ag, function by extracting electrons from CB of photocatalysts [36–38]. This seemed similar to $SrCO_3$ in the proposed system. Nevertheless, noble metals are very scarce and expensive. Fig. 14a estimated the cost of Pt and Ag to 32543 and 566 USD per kilogram, respectively. By comparison, the cost of $SrCO_3$ was only 0.58 USD per kilogram. Besides the cost, deposited noble metals may separate from the surface of the photocatalyst and cause pollution with heavy metals. Here, $SrCO_3$ formed *in situ* was difficult to separate from

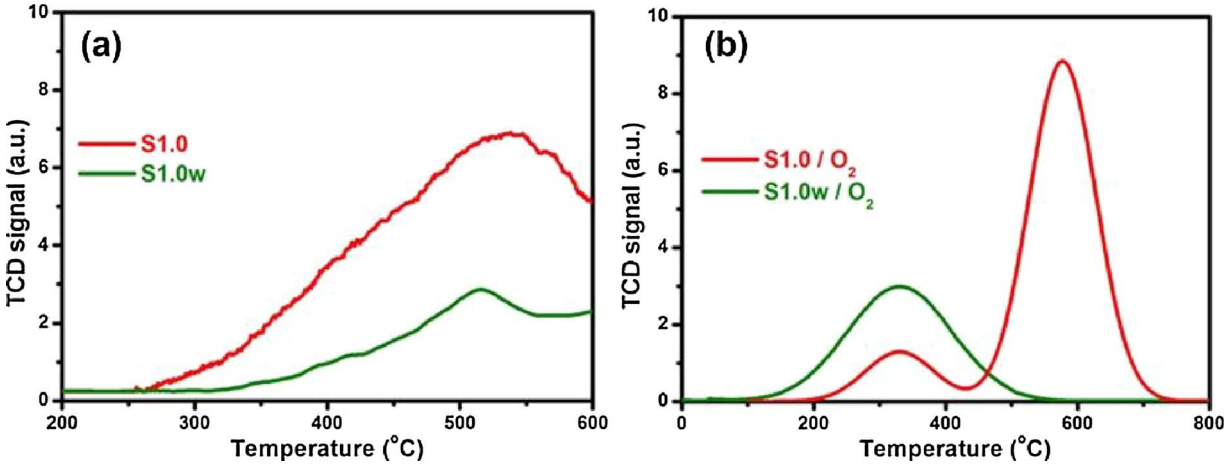

Fig. 10. NO TPD spectra (a) and O_2 TPD spectra (b) of S1.0 and S1.0w.

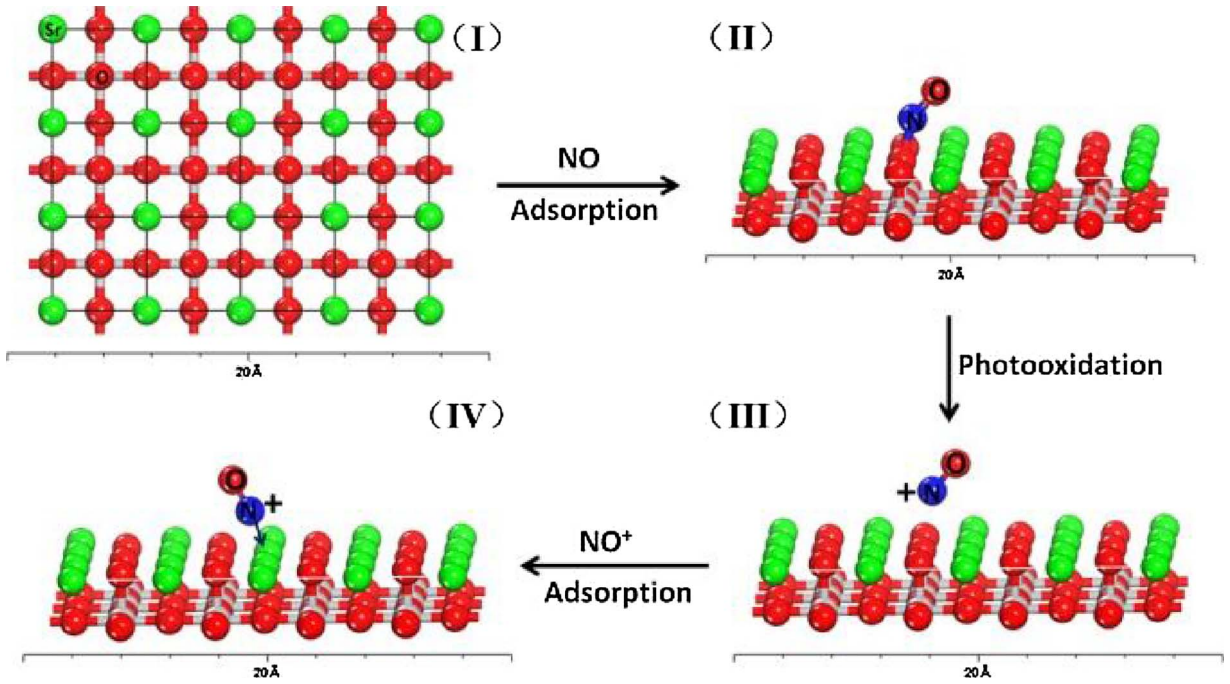

Fig. 11. The effect of the adsorption of NO on the surface of $SrTiO_3$; the red ball represents oxygen atom; the green ball represents strontium atom; the blue ball represents nitrogen atom. (For interpretation of the references to colour in this figure legend, the reader is referred to the web version of this article.)

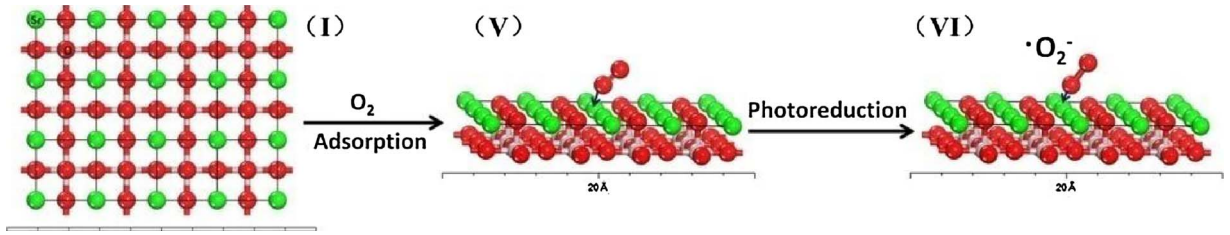

Fig. 12. The effect of the adsorption of O_2 on the surface of $SrTiO_3$; the red ball represents oxygen atom; the green ball represents strontium atom; the blue ball represents nitrogen atom. (For interpretation of the references to colour in this figure legend, the reader is referred to the web version of this article.)

the surface of $SrTiO_3$. Even if $SrCO_3$ was separated from the $SrTiO_3$ surface, $SrCO_3$ is comparably safe with no known hazards to the surrounding environment.

The activity and stability were also compared between S1.0 and noble metals modified $SrTiO_3$ (Fig. 14b). S1.0 showed the highest activity and stability among all catalysts. Although decoration with Pt and Ag could improve the NO removal activity of $SrTO_3$, deactivation of their sites linked to NO poisoning appeared more serious than $SrTO_3$. Overall, all shortcomings caused by noble metals can be avoided. Therefore, $SrCO_3$ could be used as environmentally friendly and economic substitute to noble metals.

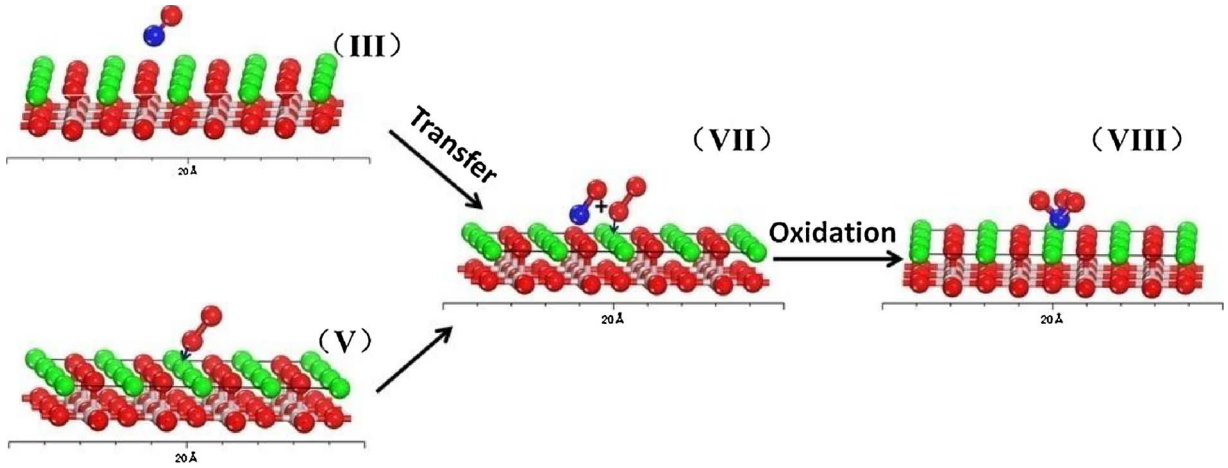

Fig. 13. The combined effect of the adsorption of NO and O_2 on the surface of $SrTiO_3$; the red ball represents oxygen atom; the green ball represents strontium atom; the blue ball represents nitrogen atom. (For interpretation of the references to colour in this figure legend, the reader is referred to the web version of this article.)

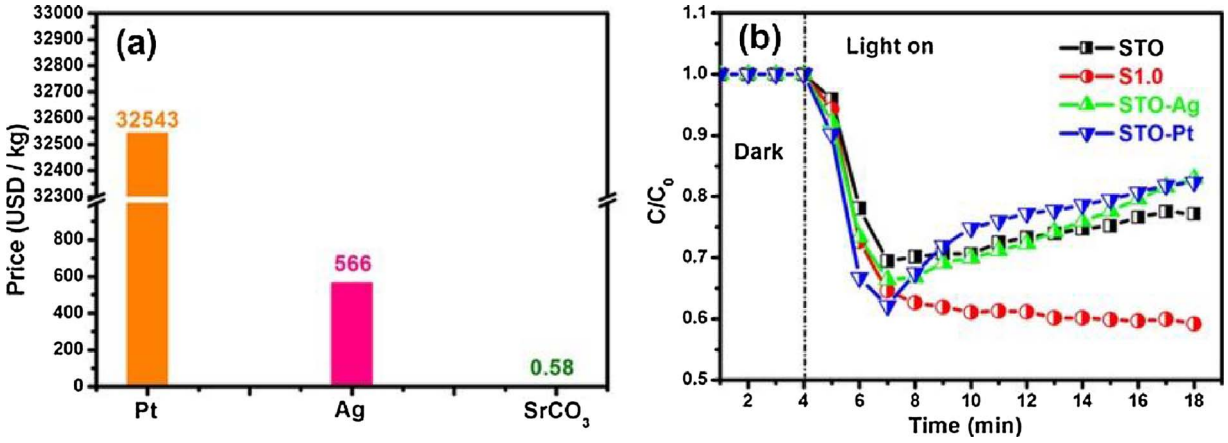

Fig. 14. The cost of Pt, Ag and $SrCO_3$ as co-catalysts (a); the activity comparison between S1.0 and noble metals (Ag and Pt) modified $SrTiO_3$ (b).

4. Conclusions

The formation mechanism of $SrTiO_3$ was examined and the data revealed that $SrTiO_3$ and $SrCO_3$ (S1.0) complexes were generated before the formation of pure $SrTiO_3$. During the photocatalytic removal process of NO, the presence of $SrCO_3$ did not only improve the photocatalytic activity of $SrTiO_3$ but also inhibited deactivation of $SrTiO_3$. On the one hand, $SrCO_3$ could improve the separation of photoinduced charge carriers of $SrTiO_3$ because CB of $SrCO_3$ could accept electrons from CB of $SrTiO_3$. This enhancement in catalytic activity was similar to that of surface deposited noble metals. In this process, $SrCO_3$ could separate the adsorption sites of NO and O_2 in two different phases, a critical role in inhibiting deactivation that could not be achieved by deposited noble metals. Moreover, $SrCO_3$ is very plentiful and cheap solving all shortcomings caused by noble metals. Therefore, $SrCO_3$ can be used as an environmently friendly and economic substitute to noble metals. Overall, these findings look promising and would pave ways to novel photocatalytic eco-materials.

Acknowledgments

Financial support by the National Nature Science Foundation of China (Grant No. 21603271) and the National “863” Project of China (No. 2015AA050502) is gratefully appreciated.

Appendix A. Supplementary data

Supplementary data associated with this article can be found, in the online version, at https://doi.org/10.1016/j.apcatb.2018.01.020.

References

[1] L.B. Kreuzer, C.K.N. Patel, Nitric oxide air pollution: detection by optoacoustic spectroscopy, Science 173 (1971) 45–47.
[2] R.J. Huang, Y. Zhang, C. Bozzetti, K.F. Ho, J.J. Cao, Y. Han, K.R. Daellenbach, J.G. Slowik, S.M. Platt, F. Canonaco, High secondary aerosol contribution to particulate pollution during haze events in China, Nature 514 (2014) 218–222.
[3] P. Granger, V.I. Parvulescu, Catalytic NOx abatement systems for mobile sources: from three-way to lean burn after-treatment technologies, Chem. Rev. 111 (2011) 3155–3207.
[4] K. Takahashi, Iron oxide cluster induced barrier-free conversion of nitric oxide to ammonia, Chem. Commun. 51 (2015) 4062–4064.
[5] G.H. Dong, D.L. Jacobs, L. Zang, C.Y. Wang, Carbon vacancy regulated photoreduction of NO to N_2 over ultrathin g-C_3N_4 nanosheets, Appl. Catal. B: Environ. 218 (2017) 515–524.
[6] C. Su, X. Ran, J. Hu, C. Shao, Photocatalytic process of simultaneous desulfurization and denitrification of flue gas by TiO_2-polyacrylonitrile nanofibers, Environ. Sci. Technol. 47 (2013) 11562–11568.
[7] H.K. Chang, G. Qi, K. Dahlberg, L. Wei, Strontium-doped perovskites rival platinum catalysts for treating NO_X in simulated diesel exhaust, Science 327 (2010) 1624–1627.
[8] W.J. Stark, K. Wegner, S.E. Pratsinis, A. Baiker, Flame aerosol synthesis of vanadia-titania nanoparticles: structural and catalytic properties in the selective catalytic reduction of NO by NH_3, J. Catal. 197 (2001) 182–191.
[9] P. Hu, Z. Huang, X. Gu, F. Xu, J. Gao, Y. Wang, Y. Chen, X. Tang, Alkali-resistant mechanism of a hollandite De-NOx catalyst, Environ. Sci. Technol. 49 (2015) 7042–7047.
[10] H. Wang, S. Gao, F. Yu, Y. Liu, X. Weng, Z. Wu, Effective way to control the performance of a ceria-based De-NOx catalyst with improved alkali resistance: acid-

base adjusting, J. Phys. Chem. C 119 (2015) 15077–15084.
[11] Z.H. Ai, W.K. Ho, S.C. Lee, L.Z. Zhang, Efficient photocatalytic removal of NO in indoor air with hierarchical bismuth oxybromide nanoplate microspheres under visible light, Environ. Sci. Technol. 43 (2009) 4143–4150.
[12] K. Fujiwara, U. Müller, S.E. Pratsinis, Pd subnano-clusters on TiO_2 for solar-light removal of NO, ACS Catal. 6 (2016) 1887–1893.
[13] Y. Huang, Y.L. Liang, Y.F. Rao, D.D. Zhu, J.J. Cao, W.K. Ho, S.C. Lee, Environment-friendly carbon quantum dots/$ZnFe_2O_4$ photocatalysts: characterization: biocompatibility and mechanisms for NO removal, Environ. Sci. Technol. 51 (2017) 2924–2933.
[14] Z.Y. Wang, Y. Huang, W.K. Ho, J.J. Cao, Z. Shen, S.C. Lee, Fabrication of $Bi_2O_2CO_3$/g-C_3N_4 heterojunctions for efficiently photocatalytic NO in air removal: in-situ self-sacrificial synthesis, characterizations and mechanistic study, Appl. Catal. B: Environ. 199 (2016) 123–133.
[15] Y.H. Li, K.L. Lv, W.K. Ho, Z.W. Zhao, Y. Huang, Enhanced visible-light photo-oxidation of nitric oxide using bismuth-coupled graphitic carbon nitride composite heterostructures, Chinese, J. Catal. 38 (2017) 321–329.
[16] G.H. Dong, L.P. Yang, F. Wang, L. Zang, C.Y. Wang, Removal of nitric oxide through visible light photocatalysis by g-C_3N_4 modified with perylene imides, ACS Catal. 6 (2016) 6511–6519.
[17] G.H. Dong, W.K. Ho, L.Z. Zhang, Photocatalytic NO removal on BiOI surface: the change from nonselective oxidation to selective oxidation, Appl. Catal. B: Environ. 168–169 (2015) 490–496.
[18] M.Y. Ou, F. Dong, W. Zhang, Z.B. Wu, Efficient visible light photocatalytic oxidation of NO in air with band-gap tailored $(BiO)_2CO_3$-BiOI solid solutions, Chem. Eng. J. 255 (2014) 650–658.
[19] F. Dong, Q.Y. Li, Y. Zhou, Y.J. Sun, H.D. Zhang, Z.B. Wu, In situ decoration of plasmonic Ag nanocrystals on the surface of $(BiO)_2CO_3$ hierarchical microspheres for enhanced visible light photocatalysis, Dalton. Trans. 43 (2014) 9468–9480.
[20] H.P. Li, Q.H. Deng, J.Y. Liu, W.G. Hou, N. Du, R.J. Zhang, X.T. Tao, Synthesis, characterization and enhanced visible light photocatalytic activity of Bi_2MoO_6/Zn-Al layered double hydroxide hierarchical heterostructures, Catal. Sci. Technol. 4 (2014) 1028–1037.
[21] F. Wang, Z.Y. Zhao, K.H. Zhang, F. Dong, Y. Zhou, Topochemical transformation of low-energy crystal facets to high-energy facets: a case from $Bi_2O_2CO_3${001} facets to β-Bi_2O_3{001} facets with improved photocatalytic oxidation of NO, CrystEngComm 17 (2015) 6098–6102.
[22] F. Dong, H.T. Liu, W.K. Ho, M. Fu, Z.B. Wu, $(NH_4)_2CO_3$ mediated hydrothermal synthesis of N-doped $(BiO)_2CO_3$ hollow nanoplates microspheres as high-performance and durable visible light photocatalyst for air cleaning, Chem. Eng. J. 214 (2013) 198–207.
[23] Y.H. Li, X.F. Wu, W.K. Ho, K.L. Lv, Q. Li, M. Li, S.C. Lee, Graphene-induced formation of visible-light-responsive SnO_2-Zn_2SnO_4 Z-scheme photocatalyst with surface vacancy for the enhanced photoreactivity towards NO and acetone oxidation, Chem. Eng. J. 336 (2018) 200–210.
[24] Y.H. Li, K.L. Lv, W.K. Ho, F. Dong, X.F. Wu, Y. Xia, Hybridization of rutile TiO2 (rTiO2) with g-C_3N_4 quantum dots (CNQDs): an efficient visible-light-driven Z-scheme hybridized photocatalyst, Appl. Catal. B: Environ. 202 (2017) 611–619.
[25] Y.H. Li, W.K. Ho, K.L. Lv, B.C. Zhu, S.C. Lee, Carbon vacancy-induced enhancement of the visible light-driven photocatalytic oxidation of NO over g-C_3N_4 nanosheets, Appl. Surf. Sci. 430 (2018) 380–389.
[26] M.S. Wrighton, A.B. Ellis, P.T. Wolczanski, D.L. Morse, H.B. Abrahamson, D.S. Ginley, Strontium trontium titanate photoelectrodes. Efficient photoassisted electrolysis of water at zero applied potential, J. Am. Chem. Soc. 7 (1976) 2774–2779.
[27] J.J. Zhu, H.L. Li, L.Y. Zhong, P. Xiao, X.L. Xu, X.G. Yang, Z. Zhao, J.L. Li, Perovskite oxides: preparation, characterizations, and applications in heterogeneous catalysis, ACS Catal. 4 (2014) 2917–2940.
[28] S. Cho, J.W. Jang, W.R. Zhang, A. Suwardi, H.Y. Wang, D.W. Wang, J.L. Macmanusdriscoll, Single-crystalline thin films for studying intrinsic properties of $BiFeO_3$-$SrTiO_3$ solid solution photoelectrodes in solar energy conversion, Chem. Mater. 27 (2015) 6635–6641.
[29] S.X. Ouyang, P. Li, H. Xu, H. Tong, L.Q. Liu, J.H. Ye, Bifunctional-nanotemplate assisted synthesis of nanoporous $SrTiO_3$ photocatalysts toward efficient degradation of organic pollutant, ACS Appl. Mater. Interfaces 6 (2014) 22726–22732.
[30] Q. Zhang, Y. Huang, L.F. Xu, J.J. Cao, W.K. Ho, S.C. Lee, Visible-light-active plasmonic Ag-$SrTiO_3$ nanocomposites for the degradation of NO in air with high selectivity, ACS Appl. Mater. Interfaces 8 (2016) 4165–4174.
[31] D. Lu, S.X. Ouyang, H. Xu, D.W. Li, X.L. Zhang, Y.X. Li, J.H. Ye, Designing Au surface-modified nanoporous-single-crystalline $SrTiO_3$ to optimize diffusion of surface plasmon resonance-induce photoelectron toward enhanced visible-light photoactivity, ACS Appl. Mater. Interfaces 8 (2016) 9506–9513.
[32] R. Konta, T. Ishii, H. Kato, A. Kudo, Photocatalytic activities of noble metal ion doped $SrTiO_3$ under visible light irradiation, J. Phys. Chem. B 35 (2004) 8992–8995.
[33] S.C. Yan, Z.S. Li, Z.G. Zou, Photodegradation of rhodamine B and methyl orange over boron-doped g-C_3N_4 under visible light irradiation, Langmuir 26 (2010) 3894–3901.
[34] G.H. Dong, W.K. Ho, Y.H. Li, L.Z. Zhang, Facile synthesis of porous graphene-like carbon nitride ($C_6N_9H_3$) with excellent photocatalytic activity for NO removal, Appl. Catal. B: Environ. 174–175 (2015) 477–485.
[35] T.T. Zhang, W.Y. Lei, P. Liu, J.A. Rodriguez, J.G. Yu, Y. Qi, G. Liu, M.H. Liu, Organic pollutant photodecomposition by Ag/$KNbO_3$ nanocomposites: a combined experimental and theoretical study, J. Phys. Chem. C 120 (2016) 2777–2786.
[36] S. Sakthivel, M.V. Shankar, M. Palanichamy, B. Arabindoo, D.W. Bahnemann, V. Murugesan, Enhancement of photocatalytic activity by metal deposition: characterisation and photonic efficiency of Pt, Au and Pd deposited on TiO_2 catalyst, Water Res. 38 (2004) 3001–3008.
[37] Z.B. Wu, Z.Y. Sheng, Y. Liu, H.Q. Wang, N. Tang, J. Wang, Characterization and activity of Pd-modified TiO_2 catalysts for photocatalytic oxidation of NO in gas phase, J. Hazard. Mater. 164 (2009) 542–548.
[38] S.K. Mohapatra, N. Kondamudi, S. Banerjee, M. Misra, Functionalization of self-organized TiO_2 nanotubes with Pd nanoparticles for photocatalytic decomposition of dyes under solar light illumination, Langmuir 24 (2008) 11276–11281.